

Microstructure Evolution in Three-Dimensional Inhomogeneous Elastic Media

XIAOFAN LI, JOHN LOWENGRUB, QING NIE, VITTORIO CRISTINI, and PERRY LEO

A new, three-dimensional boundary integral method is used to study the evolution of an isolated precipitate growing by diffusion in an infinite, elastic matrix. An adaptive surface mesh^[2,3] is used to accurately and efficiently discretize the precipitate boundaries in three dimensions. The model accounts for diffusion, surface energy, interface kinetics and elastic energy, which are coupled through a modified Gibbs–Thomson boundary condition at the precipitate–matrix interface. The precipitate and matrix phases are taken to have different elastic-stiffness tensors, and there is a mismatch strain between the phases. Both isotropic and anisotropic elasticity are investigated. In this article, the coarsening and growth of a single precipitate are simulated under various conditions. For isotropic elasticity, coarsened shapes are found to be consistent with the equilibrium-shape analysis of Johnson and Cahn.^[29] Growth shapes are found to become rapidly nonlinear and to develop regions of high curvature. In elastically anisotropic systems, coarsened shapes are found to be consistent with the equilibrium-shape calculations of Mueller and Gross.^[7,8] Simulations of coarsening in which the cubic axes of the precipitate are different from those of the matrix suggest that there may be more than one local minima in the energy, so that the observed shapes depend on the growth path. Finally, non-convex precipitate morphologies are seen for the growth of soft Ni₃Al precipitates in a Ni matrix, consistent with experimental observations. In the case of a hard Ni₃Si precipitate grown under the same conditions, we find self-similar growth of a convex shape.

I. INTRODUCTION

THE macroscopic properties of multiphase materials depend on their microstructure. In many metal alloys, this microstructure consists of individual precipitates embedded coherently in a continuous matrix phase. Such microstructures can result from a diffusional phase transformation in which a thermodynamically stable phase is driven from equilibrium by a sudden lowering of temperature. It is now established that microstructure evolution during phase transformations is influenced by the elastic fields generated by the transformation. There has been long-standing interest in simulating the diffusional evolution of these microstructures, with the ultimate aim of controlling them to achieve desired alloy properties.

Much of the numerical work in simulating phase transformations has been restricted to two-dimensional domains. However, there has been an increasing body of work performed in three dimensions. Simulations in three dimensions of phase transformations have been primarily based on either diffuse-interface methods (e.g., References 1 through 3) or the discrete-atom method.^[4,5] In these methods, microstructure evolution is mimicked through the evolution of a

smooth field (e.g., composition or a phase field) consistent with energy minimization, and, so, the methods extend readily from two to three dimensions. Wang and Khachaturyan^[1] have examined martensitic and diffusional microstructures in three dimensions using a phase-field approach. Orlikowski *et al.*^[2] have studied the effect of long-range elastic fields on the phase-separation process of both two- and three-dimensional systems with large-scale diffuse-interface simulations. Lee^[4,5] has applied the discrete-atom method to simulate phase separation in three dimensions.

Three-dimensional simulations using sharp-interface models are more difficult, in part because these methods require tracking a mathematically sharp interface. Thompson and Voorhees^[6] and Mueller and Gross^[7,8] have used sharp-interface models to find equilibrium shapes by minimizing the total energy, which is the sum of the elastic and surface energies. However, to our knowledge, there has not been any work in which a sharp-interface formulation is used to track evolving precipitate shapes in three dimensions. Such a formulation allows for a precise description of precipitate shapes and provides a numerical validation to the diffuse-interface and discrete-atom methods discussed previously. Also, the boundary integral formulation only requires fields on the precipitate–matrix interface and not everywhere in the system. This reduction in the dimensionality of the problem may, in some applications, give the sharp-interface approach a computational advantage over other approaches.

In this work, we simulate the full diffusional evolution of an isolated three-dimensional precipitate embedded in infinite matrix phase, based on a sharp-interface formulation of the problem. Diffusion is assumed to be quasi-steady in both the precipitate and matrix phases. The precipitate and matrix are taken to be linearly elastic, with different elastic properties. Elastic fields are generated by a misfit strain between the phases and are assumed to satisfy the equations

XIAOFAN LI is with the Department of Applied Mathematics, Illinois Institute of Technology, Chicago, IL 60616. JOHN LOWENGRUB, formerly with the School of Mathematics, University of Minnesota, Minneapolis, MN 55455 is now with the Department of Math, University of California at Irvine, Irvine, CA 92697. Contact e-mail: lowengrb@math.uci.edu QING NIE is with the Department of Mathematics, University of California-Irvine, Irvine, CA 92697-3875. VITTORIO CRISTINI, formerly with the Department of Chemical Engineering and the School of Mathematics, University of Minnesota, is with the Department of Biomedical Engineering, Rockwell Engineering Center, University of California-Irvine, Irvine, CA 92697-2715. PERRY LEO is with the Department of Aerospace Engineering and Mechanics, University of Minnesota, Minneapolis, MN 55455.

Manuscript submitted October 1, 2002.

of elastic equilibrium. The precipitate-matrix interface is a closed, two-dimensional, sharp (zero-thickness) surface with isotropic surface energy and isotropic interfacial kinetics. The boundary condition for the composition on the interface is a generalized Gibbs–Thomson condition accounting for surface energy, elastic energy, and interfacial kinetic effects. This boundary condition provides all the coupling between the elastic fields and the diffusion fields. Finally, the growth of the precipitate is determined by a far-field condition in which either the far-field composition or the mass flux into the system is prescribed.

In Section II, the governing equations and boundary integral formulations are described. In Section III, the numerical techniques for the moving-boundary problem are presented. In Section IV, the convergence and accuracy of the numerical methods in solving the boundary integral equations are discussed. In Section V, the numerical method is used to generate both equilibrium and growing precipitate shapes of precipitates for different sets of elastic parameters. Finally, in Section VI, the results are discussed and some conclusions are drawn.

II. GOVERNING EQUATIONS

We consider the formation of a two-phase microstructure in a binary alloy. The matrix phase (Ω^M) extends to infinity, while the precipitate phase (Ω^P) consists of an isolated particle occupying a finite volume. The interface between the two phases is a closed surface ($\partial\Omega$).

The evolution of the precipitate-matrix interface is controlled by diffusion of matter across the interface. As we assume quasi-static diffusion, the normalized composition (c) is governed by Laplace’s equation, $\Delta c = 0$, in both phases. The composition on the precipitate-matrix interface is given by

$$c = -\kappa - Zg^{el} - \lambda v_n \quad \text{on} \quad \partial\Omega \quad [1]$$

where κ is the total curvature of the interface, the constant Z characterizes the relative contribution of the elastic and surface energies,^[9] g^{el} is an elastic-energy density defined in Eq. [5], v_n is the normal velocity of the precipitate-matrix interface, and λ is a nondimensional kinetic coefficient. We assume for simplicity that the diffusivities of the two phases are identical; therefore, the normal velocity (v_n) is given by the flux balance

$$v_n = \left. \frac{\partial c}{\partial \mathbf{n}} \right|_{\partial\Omega^+} - \left. \frac{\partial c}{\partial \mathbf{n}} \right|_{\partial\Omega^-} \quad [2]$$

where \mathbf{n} is the outward-pointing unit normal of the interface and $(\partial c/\partial \mathbf{n})|_{\partial\Omega^+}$ and $(\partial c/\partial \mathbf{n})|_{\partial\Omega^-}$ denote the values of the normal derivative of c evaluated on the precipitate side and the matrix side of the interface, respectively.

Following References 10 and 11, we consider two different far-field conditions for the diffusion problem. In the first, the mass flux (J) into the system is specified:

$$J = \frac{1}{4\pi} \iint_{\partial\Omega} v_n dA = J_\infty \quad [3]$$

In the second, the far-field composition (c_∞) is specified:

$$\lim_{|x| \rightarrow \infty} c = c_\infty \quad [4]$$

Because of the g^{el} term in the boundary condition [1], one must solve for the elastic fields in the system before finding the diffusion fields. The elastic fields arise because of a misfit strain, denoted by ϵ^T , between the precipitate and matrix. Following the work of Eshelby,^[12] this misfit is taken into account through the constitutive relations between the stress (σ_{ij}) and strain (ϵ_{ij}). These are $\sigma_{ij}^P = C_{ijkp}^P (\epsilon_{kp}^P - \epsilon_{kp}^T)$ in the precipitate and $\sigma_{ij}^M = C_{ijkp}^M \epsilon_{kp}^M$ in the matrix. The elastic-stiffness tensor (C_{ijkp}) may be different in the matrix and precipitate (elastically inhomogeneous). We note also that C_{ijkp} can reflect different material symmetries of the two phases.

The equations of elastic equilibrium require that $\sigma_{ij,j} = 0$ in both phases (in the absence of body forces). We assume the interface $\partial\Omega$ to be coherent, so the displacement (\mathbf{u}) and the traction (\mathbf{t}) are continuous across it. For simplicity, we suppose that the far-field tractions and displacements vanish, although it is straightforward to include them in the formulation. Finally, the elastic-energy density in the boundary condition [1] is computed as

$$g^{el} = \frac{1}{2} (\sigma_{ij}^P (\epsilon_{ij}^P - \epsilon_{ij}^T) - \sigma_{ij}^M \epsilon_{ij}^M) \quad [5]$$

$$+ \sigma_{ij}^M (\epsilon_{ij}^M - \epsilon_{ij}^P) \quad \text{on} \quad \partial\Omega$$

The model just presented differs from the two-dimensional model presented in References 9 and 13 in two ways. First, the kinetic term in the boundary condition [1] was not included in the two-dimensional boundary integral calculations of References 9 and 13, where the boundary was taken to be in local equilibrium ($\lambda = 0$). However, interfacial kinetics are often included in models of phase transitions.^[10,11] Second, the model considered here allows diffusion in both the matrix and precipitate phases, whereas only diffusion in the matrix was considered in References 9 and 13. For simplicity, we have assumed that the diffusivities of both phases are identical, although different diffusivities could easily be incorporated in the flux balance [2]. Also, the boundary condition [1] holds on both sides of the interface. We note that the composition is normalized differently in the precipitate and matrix, so that the normalized composition is continuous across the interface (the actual composition undergoes a jump).

The total energy of the system (W_{tot}) is the sum of the surface energy (W_s) and the elastic energy (W_e), where

$$W_s = \iint_{\partial\Omega} dA, \quad W_e = \frac{Z}{2} \left(\iint_{\Omega^P} \sigma_{ij}^P (\epsilon_{ij}^P - \epsilon_{ij}^T) dV \right. \quad [6]$$

$$\left. + \iint_{\Omega^M} \sigma_{ij}^M \epsilon_{ij}^M dV \right)$$

For a coherent interface and a uniform misfit strain, it is well known that the elastic energy can be written as a boundary integral:^[12]

$$W_e = -\frac{Z}{2} \iint_{\partial\Omega} t_i \epsilon_{ik}^T x_k dA_x \quad [7]$$

Finally, the boundary integral equations for the diffusion and elasticity problems have been presented in detail in previous works^[9,13] in two dimensions. In three dimensions, the integral-equation formulations have the same structure as their two-dimensional counterparts, except that the Green's functions are different. We note that since the diffusivities of the phases are matched, the diffusion integral equation is posed for the normal velocity directly (*e.g.*, Reference 14), rather than for a dipole-layer potential, as in References 15, 9, and 13.

A. Desingularized Integral Equations for Elasticity

The boundary integral equations for the continuous-displacement field ($\mathbf{u}(\mathbf{x})$), and traction field ($\mathbf{t}(\mathbf{x})$) on the interface involve Cauchy-principal-value integrals over the interface.^[16,9] In our numerical calculations, we found it necessary to implement a new desingularized form of these integral equations, in which the principal-value integrals are eliminated. These integral equations can be obtained by using the identity

$$PV \iint_{\partial\Omega} T_{ijk}(\mathbf{y} - \mathbf{x}) n_k(\mathbf{y}) dA_y = -\frac{1}{2} \delta_{ij}, \quad \text{for } \mathbf{x} \in \partial\Omega \quad [8]$$

where PV denotes the principal-value integral and T_{ijk} is the Green's function associated with the traction. This identity yields the desingularized form of the elasticity integral equations,

$$\begin{aligned} & \iint_{\partial\Omega} (u_i(\mathbf{y}) - u_i(\mathbf{x})) T_{ijk}^P(\mathbf{y} - \mathbf{x}) n_k(\mathbf{y}) dA_y - \iint_{\partial\Omega} t_i(\mathbf{y}) G_{ij}^P(\mathbf{y} - \mathbf{x}) dA_y \\ & = \iint_{\partial\Omega} t_i^T(\mathbf{y}) G_{ij}^P(\mathbf{y} - \mathbf{x}) dA_y, \quad j = 1, 2, 3, \\ & u_j(\mathbf{x}) - \iint_{\partial\Omega} (u_i(\mathbf{y}) - u_i(\mathbf{x})) T_{ijk}^M(\mathbf{y} - \mathbf{x}) n_k(\mathbf{y}) dA_y \\ & \quad + \iint_{\partial\Omega} t_i(\mathbf{y}) G_{ij}^M(\mathbf{y} - \mathbf{x}) dA_y = 0 \end{aligned} \quad [9]$$

where G_{ij} is the Green's function associated with the displacement, and $t_i^T = C_{ijkp}^P \epsilon_{kp}^T n_j$ is the misfit traction.

B. Green's Functions

The Green's functions G_{ij} and T_{ijk} for isotropic elastic materials are given by the Kelvin solution.^[17] These functions are evaluated directly in our simulations of isotropic materials.

However, it is well known that in three dimensions, the Green's functions for general anisotropic materials cannot be expressed explicitly and, rather, are written in terms of line integrals (*e.g.*, References 18 through 20). In our simulations, the line integrals, which are smooth and doubly periodic functions of two independent variables (θ_1 and θ_2), are tabulated and stored in two-dimensional arrays. To evaluate the line integrals at an arbitrary point (θ_1 , θ_2), we use

the values of the 16 table entry points that are closest to the point and interpolate with standard-product Lagrangian polynomials. The average relative error due to the interpolation was determined to be of the order of 10^{-5} over the whole domain of the independent variables. The size of the two-dimensional tabulation array necessary to achieve this level of accuracy was 129×259 . The repeated computation of the line integrals is avoided, and the computational cost is reduced drastically. We obtain a reduction in central processing unit time by a factor of 170 with respect to that required for the direct evaluation of the Green's functions. Similar but less accurate techniques are used in previous studies.^[21,6,7]

III. NUMERICAL METHODS

We briefly describe the numerical procedures for solving the diffusional evolution of the inhomogeneous system. The details will be published elsewhere. For a given precipitate shape, we first obtain the displacement and the traction on the interface by solving the elasticity equations [9] using the tabulated values of the Green's function, described previously. An adaptive surface triangulation,^[22,23] described briefly as follows, is used to represent the interface. Then, the elastic-energy density is calculated and the diffusion equation is solved to determine the normal velocity. Finally, the surface is evolved one time step, using \mathbf{v}_n , the surface is remeshed, and the process is repeated.

The integral equations are solved using the collocation method together with the GMRES iterative method.^[24] The number of iterations required to solve the systems depends on the interface morphology, but is insensitive to the mesh size for a fixed surface morphology. The overall integral-equation algorithm is similar to that described in Reference 25 for the diffusion equation, although here our specific application is different and, thus, the details of the algorithms are different. We found that by storing the full diffusion and elasticity matrices, the matrix-vector products used in GMRES could be performed much more efficiently (a speed-up of at least a factor of 4) than if the matrices are not stored. This is because when the matrix is not stored, the matrix elements are essentially recomputed every time the matrix-vector product is performed. Storing the full matrix does impose some memory limitations when a large number of points is used to discretize the complex surface morphologies of the precipitates.

In the discretization, local quadratic Lagrange interpolation is used to represent field quantities (*i.e.*, \mathbf{u} , \mathbf{t} , \mathbf{v}_n , and the position of the interface \mathbf{x}) in triangle interiors. The normal vector is derived from the local coordinates using the Lagrange interpolants of the interface position. The curvature is determined by performing a local paraboloid fit to the triangulated surface.^[26] This combination was found to yield the best accuracy for a given resolution.

On mesh triangles where the integrand is singular, a non-linear change of variables (Duffy's transformation^[25]) is used to map the singular triangle to a unit square and to remove the $1/r$ divergence of the integrand. The ten-point (in each direction) Gauss-Legendre quadrature rule is then used to perform the integration on the unit square. For triangles in a region close to the singular triangle, the integrand is nearly singular, and, so, each of these triangles is divided into four smaller triangles, and a fifth-order quadrature^[27] is used

on each subtriangle individually. On all other mesh triangles, the fifth-order quadrature is used to approximate the integrals.

To compute the elastic-energy density defined in Eq. [5], we need to determine all of the components of the stress and strain tensors σ and ϵ , on both sides of the interface. Following the procedure outlined in Reference 9, the necessary quantities are obtained from \mathbf{u} and \mathbf{t} , the elastic constants, and a set of local coordinates along the interface.

A second-order Runge–Kutta method is used to advance the triangle nodes

$$\frac{dx_i}{dt} = v_i \mathbf{n}, \quad i = 1, \dots, n_v \quad [10]$$

where n_v is the total number of computational nodes. The time-step size Δt is proportional to the smallest diameter of the triangular elements h , *i.e.*, $\Delta t = Ch$. The constant factor C depends on the physical parameters of the system and is typically set in the range of $0.005 \leq C \leq 0.01$.

Since the shape of the precipitate can change substantially during its evolution, an adaptive-mesh algorithm^[22,23] is used to achieve accurate and efficient simulations. In this algorithm, the solid angle is uniformly resolved throughout the simulation using the following local-mesh restructuring operations to achieve an optimal mesh density: grid equilibration, edge-swapping, and node addition and subtraction. This results in a density of node points that is proportional to the maximum of the curvature (in absolute value), so that grid points cluster in highly curved regions of the interface. Further, each of the mesh triangles is nearly equilateral.

In our algorithm, we remesh every N_r time steps, or when the change of the surface area of the precipitate, compared with the surface area at the previous grid adjustment, exceeds a prescribed percentage (tol_s). Typically, in our simulations, the parameters N_r and tol_s are chosen to be 25 and 0.2 pct, respectively.

Finally, an efficient parallelization algorithm is implemented for the diffusion and elasticity solvers. The computational strategy for the parallelization is similar to the one designed for the microstructural evolution in two-dimensional elastic media.^[13] A new feature of the algorithm implemented here is that the diffusion and elasticity matrices are also divided among the different processors in order to reduce the amount of memory required on each individual processor.

IV. NUMERICAL VALIDATION

We demonstrate the convergence and accuracy of the numerical methods by considering the case where the precipitate and matrix are both isotropic, although with different elastic constants. For ellipsoids of revolution, Barnett *et al.*^[28] have computed the total energy as a function of aspect ratio, and Johnson and Cahn^[29] have computed, for a given volume, the equilibrium shape (minimum total energy shape). Johnson and Cahn have shown that when the shear modulus of the precipitate is less than that of the matrix, the equilibrium shape jumps from a sphere to an ellipsoid of revolution at a critical value of the parameter Z in Eq. [1].

We use the Johnson and Cahn analysis and result to validate our numerical scheme. Consider a spheroid with the

semiaxes a , a , and b along the x_1 -, x_2 -, and x_3 -axes, respectively. Define a shape parameter by $\rho = (b/a)^{1/3}$. We take the case where the dimensionless shear moduli (scaled by the shear modulus in the matrix) are $\mu^P = 0.5$ in the precipitate and $\mu^M = 1$ in the matrix, while the Poisson ratios are $\nu^P = \nu^M = 0.25$. We also take a dilatational misfit of $\epsilon_{ij} = \delta_{ij}$, $Z = 6.4$, an initial precipitate volume of $V_0(\Omega^P) = 4\pi/3$, and a far-field flux of $J = 0$. For these parameters, the transition from sphere to ellipsoid is possible above a critical value of $Z_c \approx 5.7$.

Figure 1 shows the simulation results for ρ as a function of time for different numbers of triangular mesh elements: $n_f = 230, 420$, and 740 . An analogous plot can be made for the total energy, although it is not presented here. The initial shape is a spheroid with $\rho = 0.76$. The precipitate reaches an equilibrium shape for each grid size, with the equilibrium values of ρ and W_{tot} converging to values that are slightly less than the Johnson–Cahn analytical predictions. Specifically, at the finest grid size, $\rho = 0.71248$ and $W_{\text{tot}} = 74.1134$, while the Johnson–Cahn result (shown as the open circle in Figure 1(a) gives $\rho = 0.7188$ and $W_{\text{tot}} = 74.1163$ for the equilibrium shape. We note that analytically, there are only very small differences in total energy for spheroids with $0.7 < \rho < 1$. For example, the total energy at $\rho = 0.71$ is 74.1186 , about 3×10^{-5} larger than the minimum total energy. Thus, accurate numerical methods are required to obtain the precise equilibrium shape by simulating the full diffusional dynamics. In addition, the analytical results are restricted to ellipsoids of revolution, while the numerical simulation allows arbitrary shapes.

Convergence of the scheme is shown in Figure 1(b), in which the error in the equilibrium-shape parameter (ρ^{eq}) is plotted for different numbers of triangular elements on the surface. The plot shows four different resolutions corresponding to $n_f = 230, 322, 420$, and 740 triangular elements. The value of ρ^{eq} at the finest grid size of $n_f = 740$ is taken as the exact value in computing the errors. The horizontal scale is $1/740 - 1/n_f$. The convergence appears to be close to $O(1/n_f)$. Finally, Figure 1(c) shows the equilibrium shape of the precipitate at the end of the simulation, with $n_f = 420$. For clarity, each curved triangular element is represented by connecting the midpoints of each (flat) surface triangle. As expected, the equilibrium shape is approximately an ellipsoid of revolution. Note also that the adaptive-mesh algorithm adds more elements on the interface in the regions of large curvature.

V. SIMULATION RESULTS

We present results from simulations of coarsening and growing precipitates. For coarsening precipitates the far-field flux is zero, while for growing precipitates either the far-field flux is positive or the far-field composition is set so that the precipitate grows. We begin by considering the case where the precipitate and matrix are both elastically isotropic, but with different elastic constants. We then consider the anisotropic, inhomogeneous case.

A. Isotropic Elasticity

Consider the evolution of a precipitate growing from a unit sphere with a misfit of $\epsilon^T = \text{diag}(1, -1, 0)$. We choose this misfit because in the isotropic case, a nondilatational

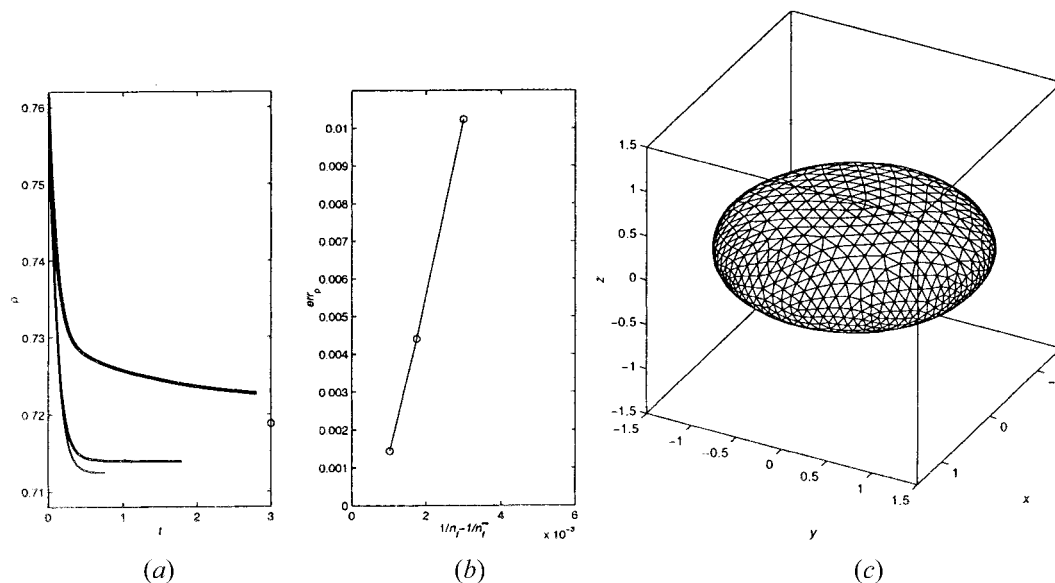


Fig. 1—(a) The time evolution of the shape parameter ρ from the numerical simulation is shown as a function of time for different numbers of triangular mesh elements, n_f . (b) The error in the equilibrium shape parameter, ρ^{eq} , is plotted for different numbers of triangular elements on the surface. The value of ρ^{eq} at the finest grid size, $n_f = 740$, is taken as the exact value in computing the errors. (c) The shape of the precipitate is shown at the end of the simulation with 420 triangular elements. The parameters for all the figures are $V_0(\Omega^P) = 4\pi/3$, $Z = 6.4$, $\mu^P = 0.5$, $\mu^M = 1$, $\nu^P = 0.5$, $\nu^M = 0.25$, and $\epsilon^T = \text{diag}(1, 1, 1)$.

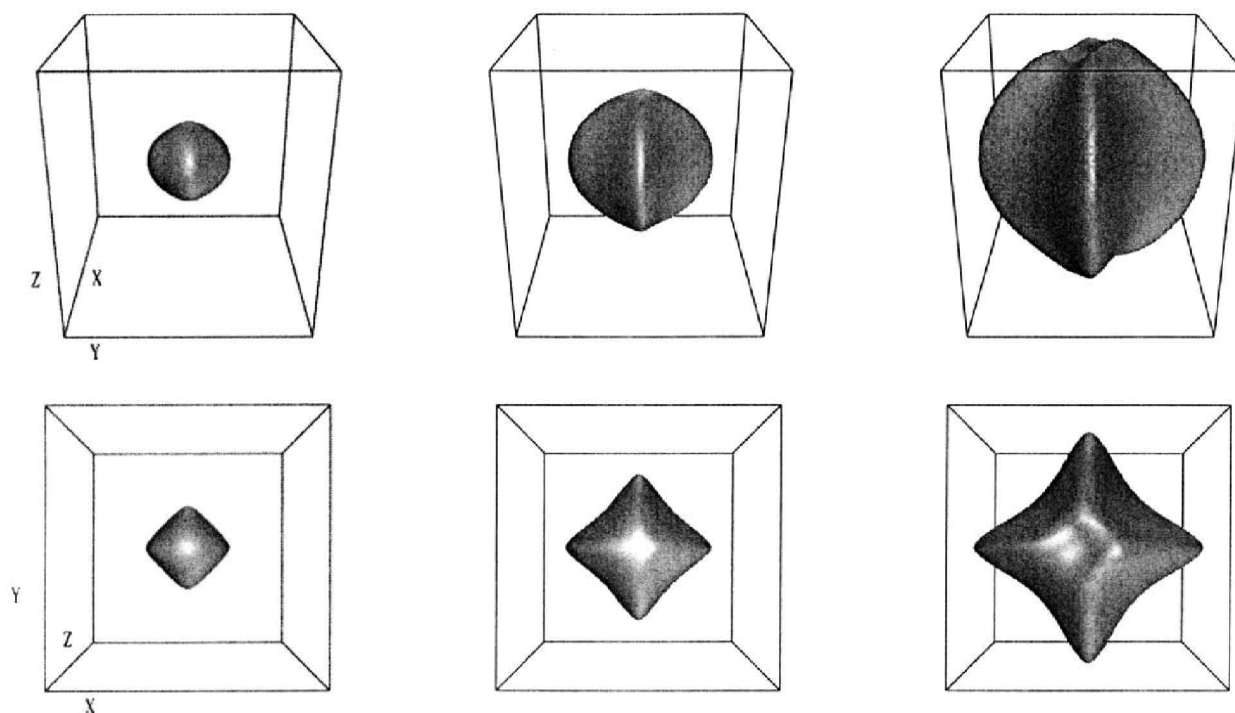


Fig. 2—Time sequence of precipitate shapes from a unit sphere with $J = 81$, $Z = 2$, elastic constants $\mu^P = 0.5$, $\mu^M = 1$, $\nu^M = 1$, $\nu^P = \nu^M = 0.25$, and the misfit $\epsilon^T = \text{diag}(1, -1, 0)$. The top row shows three-dimensional views of the precipitate as it grows, while the bottom row shows the same precipitates viewed from the positive z -axis. The times for each column are $t = 0.18$, $t = 0.815$, and $t = 2.885$.

misfit or applied field is needed to break spherical symmetry before the onset of morphological instability.^[30,9] In particular, the misfit $\epsilon^T = \text{diag}(1, -1, 0)$ allows for the existence of invariant planes with normals $(\pm 1, \pm 1, 0)$, and, so, the precipitate can lower its energy by facetting along these directions. Also, we take $\mu^P = 0.5$, $\mu^M = 1$, and $\nu^P = \nu^M = 0.25$.

We simulate particle growth using either flux or composition far-field conditions. Consider first a constant far-field flux J . Figure 2 shows the precipitate evolution with $Z = 2$ and $J = 81$. The top row shows a three-dimensional view, while the second row shows a view from the positive z -axis. The flux $J = 81$ is chosen because it is the highest flux for which a fourth-mode spherical harmonic is linearly stable

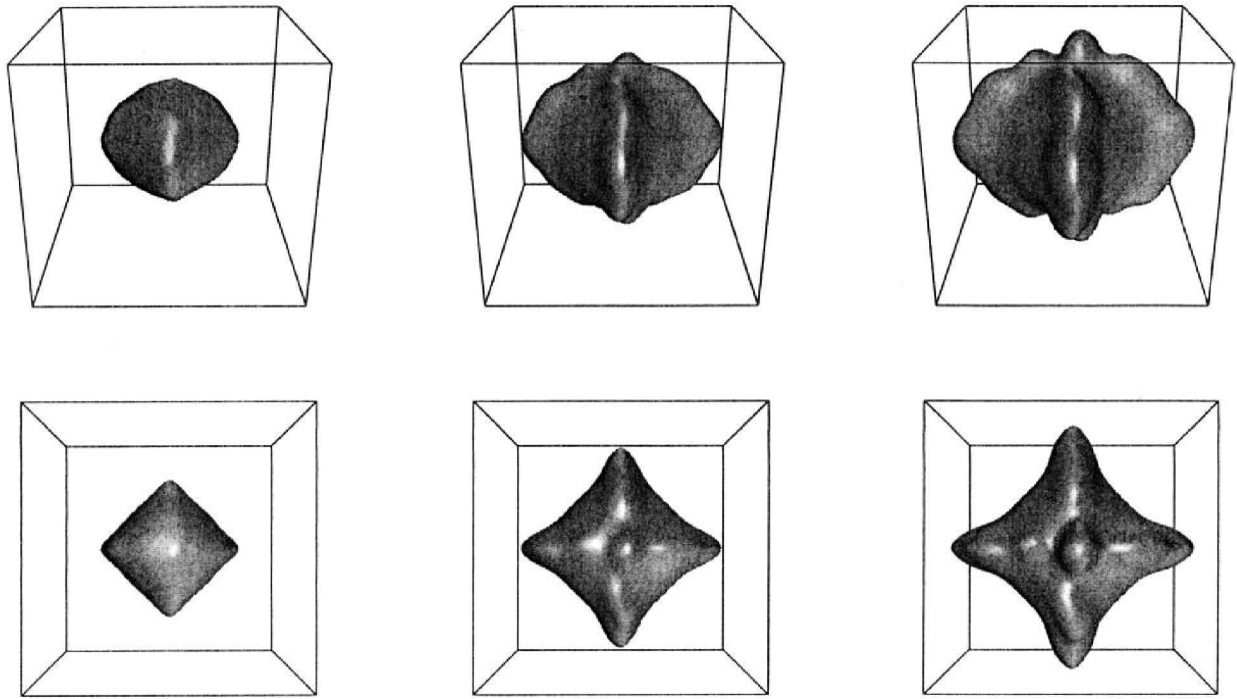


Fig. 3—Time sequence of precipitate shapes from a unit sphere with $c_\infty = -92.54$, $Z = 2$, elastic constants $\mu^p = 0.5$, $\mu^M = 1$, $\nu^p = \nu^M = 0.25$, and the misfit $\epsilon^T = \text{diag}(1, -1, 0)$. The views are the same as in Fig. 2. The times for each column are $t = 0.11$, $t = 0.18$, and $t = 0.25$.

when $Z = 0$ (Reference 10 provides details). At early times, the precipitate shape is cuboidal with convex sides. As evolution proceeds, the high-curvature edges of the particle grow outward, so that the particle takes on a star shape. That is, the principal directions of the misfit-strain tensor grow faster than the other directions. This shape, when viewed in the x - y plane, is consistent with the two-dimensional calculations of Jou and co-workers.^[9,30]

Consider next a fixed far-field composition. Figure 3 shows growth under the far-field composition $c_\infty = -92.54$, which corresponds to an initial flux of $J = 81$. All other parameters, and the views, are the same as in Figure 2. We observe that the unstable modes are more pronounced in Figure 3 compared to those seen in Figure 2. This reflects the fact that when c_∞ is fixed and the particle size increases, the flux into the system also increases.^[10] The unstable modes quickly grow into the nonlinear regime, leading to fairly complicated growth shapes at later times. However, the four fold perturbation still dominates, as it is driven by the elastic energy.

In these computations, the adaptive-mesh algorithm increases the number of triangles from 320 at $t = 0$ to 1604 at the final stage of the simulations. Figure 4 shows the detailed mesh for the final shape of the constant far-field composition case. The simulation is stopped when the mesh size increases beyond the memory capacity needed to store the full diffusion and elasticity matrices.

B. Anisotropic Elasticity

Consider next the case where both the precipitate and matrix phases are elastically anisotropic. As discussed previously, the three-dimensional Green's function for anisotropic elasticity is tabulated numerically to speed up the compu-

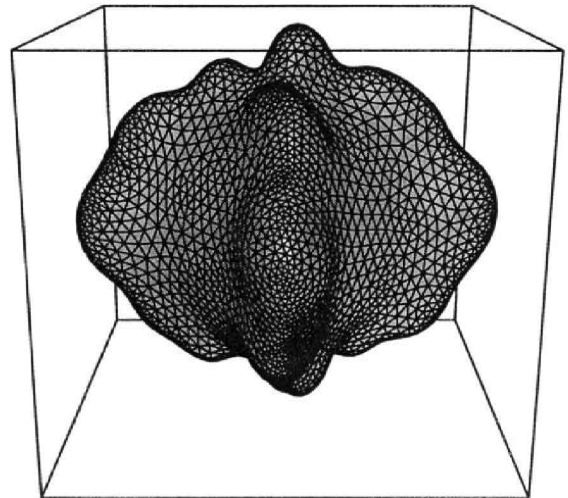


Fig. 4—The detailed mesh for the final shape ($t = 0.25$) of the constant far-field composition case shown in Fig. 3.

tation. We use elastic constants appropriate to either a Ni_3Al or a Ni_3Si precipitate embedded in a nickel matrix.^[31] In Voigt notation, the elastic constants for nickel are $c_{11} = c_{22} = c_{33} = 2.03$, $c_{12} = c_{13} = c_{23} = 1.21$, and $c_{44} = c_{55} = c_{66} = 1$; those for Ni_3Al are $c_{11} = c_{22} = c_{33} = 1.83$, $c_{12} = c_{13} = c_{23} = 1.21$, and $c_{44} = c_{55} = c_{66} = 1.02$; and those for Ni_3Si are $c_{11} = c_{22} = c_{33} = 3.04$, $c_{12} = c_{13} = c_{23} = 1.62$, and $c_{44} = c_{55} = c_{66} = 1.35$. These constants are normalized by the value of c_{44} of the matrix phase. Note that the effective shear modulus $\bar{\mu} = (c_{11} + c_{22} + c_{33} - c_{12} - c_{23} - c_{13} + 3(c_{44} + c_{55} + c_{66}))/15$ is 0.764 for nickel 0.736 for Ni_3Al , and 1.094 for Ni_3Si ; hence, the Ni_3Al precipitate

is elastically “softer” than the matrix, while the Ni_3Si precipitate is elastically “harder” than the matrix. Also, in all three materials, the anisotropy is such that the axial ($\langle 100 \rangle$ -type) directions are less stiff than the diagonal ($\langle 111 \rangle$ -type) directions. Finally, because the elastic anisotropy will drive the precipitate shape away from a sphere, we consider a dilatational misfit of $\epsilon^T = \text{diag}(1, 1, 1)$.

We consider first the coarsening dynamics of a precipitate toward its equilibrium shape by setting the far-field flux $J = 0$. Define a new shape parameter, ρ^* , by

$$\rho^* = \left(\frac{d_{\min}}{d_{\max}} \right)^{1/3} \quad [11]$$

where d_{\min} and d_{\max} are the minimum and maximum diameters of the precipitate. Figure 5 shows the evolution of the shape parameter ρ^* and the total energy W_{tot} for a Ni_3Al -Ni system with $Z = 4$. Two initial shapes were considered: a sphere with $\rho^* = 1$ (solid curve) and an ellipsoid with $\rho^* = 0.8$ (dashed curve). At time $t = 0.08$, the sphere has evolved to a cuboid (Figure 5(c)), which is associated with a plateau in the energy. This cuboidal shape is not stable and continues to evolve to an oblate cuboid (Figure 5(d)). The initial ellipsoid evolves more rapidly toward the same oblate cuboid. These results are consistent with the stability calculations of Mueller and Gross,^[7] who predicted a cuboid-to-oblate cuboid transition for a large particle size. However, they were unable to obtain stable oblate shapes in the absence of external loading.^[8]

The equilibrium shape for the hard Ni_3Si precipitate can also be found by evolving with $J = 0$. The Ni_3Si particle evolves toward a cuboid (not shown) for any initial shape, in agreement with equilibrium-shape calculations.^[7]

One of the advantages of the sharp-interface method is that it allows for complete control over the system's parameters. As an example, we study precipitate evolution as a function of the crystallographic orientation relationship between the precipitate and the matrix. We again take the Ni_3Al -Ni system with dilatational misfit, but we allow their cubic axes to be misaligned. Specifically, take the coordinate system (x, y, z) along the cube directions of the matrix, *i.e.*, $\langle 100 \rangle$, $\langle 010 \rangle$, and $\langle 001 \rangle$. We take the cubic directions of the precipitate to be rotated by an angle ξ in a plane with the normal $\mathbf{n} = \langle 0\bar{1}1 \rangle$. From the cubic symmetry, the dependence on ξ is 180 deg periodic and symmetric about 90 deg. When $\xi = 0$ deg, the cubic axes of the precipitate and the matrix are aligned, and we recover the results just discussed.

Figure 6 shows coarsened precipitate shapes as a function of ξ . The precipitates are platelike for all ξ values, although the orientation depends on ξ . The precipitate shape in Figure 6(a) corresponding to $\xi = 30$ deg was generated using the initial shape given in Figure 5(d). Figures 6(b), $\xi = 54.7$ deg, and 6(c), $\xi = 90$ deg, were generated using the initial shapes in Figures 6(a) and 6(b), respectively. In Figure 6(d), $\xi = 90$ deg again, but the initial shape is taken to be a unit sphere. In Figures 6(a) through (c), the precipitate orientations vary smoothly. In Figure 6(d) however, both the orientation and shape are quite different from the

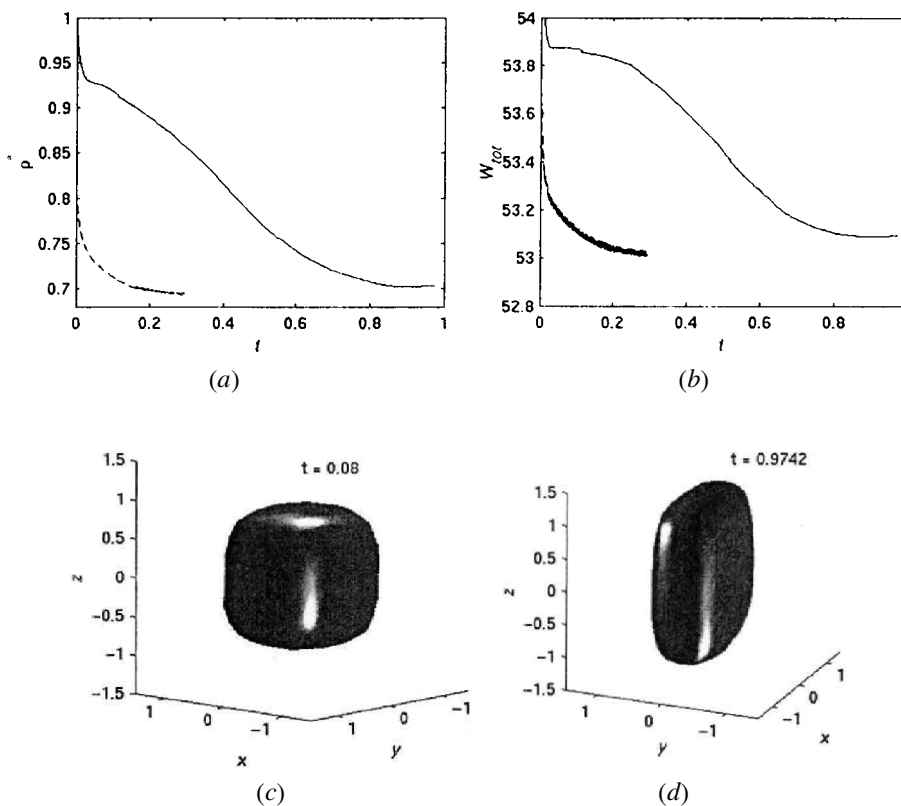


Fig. 5—(a) The evolution of the shape parameter ρ^* for a Ni_3Al precipitate in a nickel matrix. The solid line is obtained for evolution from a unit sphere, while the dashed line is from a spheroidal shape with the same volume. Also, the flux $J = 0$, $Z = 4$, and the misfit $\epsilon^T = \text{diag}(1, 1, 1)$. (b) The same as (a) except for the total energy W_{tot} . (c) The precipitate shape at time $t = 0.08$ as evolved from the unit sphere. (d) The precipitate shape at equilibrium.

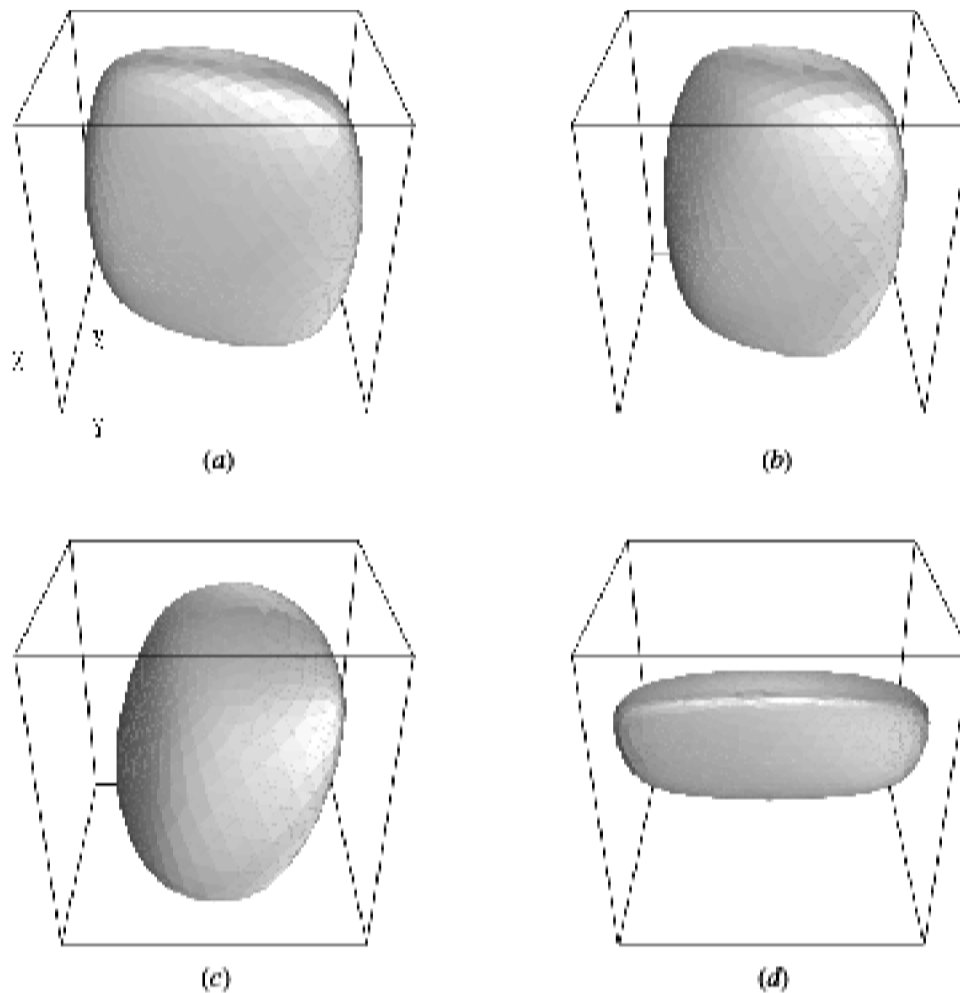


Fig. 6—The coarsened shapes of the Ni_3Al precipitates in a nickel matrix as the crystallographic directions of the precipitate are rotated by an angle ξ in a plane with the normal $\mathbf{n} = \langle 011 \rangle$: (a) $\xi = 30$ deg, (b), $\xi = 54.7$ deg, and (c) and (d) $\xi = 90$ deg. The precipitates in (c) and (d) were generated using different initial shapes as described in the text. In these simulations, $V_0(\Omega^p) = 4\pi/3$, $J = 0$, $Z = 4$, and $\epsilon^T = \text{diag}(1, 1, 1)$.

precipitate shown in Figure 6(c). Also, the total energy in Figure 6(d) is only slightly smaller than that in Figure 6(c): 53.605 for Figure 6(d) and 53.895 for Figure 6(c). This suggests that there may be multiple local minima for $\xi = 90$ deg. Further simulations suggests that this may be true for other values of ξ , and this is currently under study.

We conclude by considering the growth of a precipitate when both the precipitate and matrix phases are elastically anisotropic. As stated earlier, the misfit strain is dilatational, and we consider both a Ni_3Al and a Ni_3Si precipitate. Figures 7(a) through (c) show the growth of an initially unit spherical Ni_3Al precipitate with $Z = 4$ and a constant-flux far-field of $J = 81$. The growing Ni_3Al precipitate develops nonconvex faces. Such nonconvex morphologies have been observed experimentally by Yoo *et al.*^[32] in a model nickel superalloy system (Figure 7(d)).

Figures 8(a) through (c) show the growth of a Ni_3Si precipitate under the same conditions. In this case, the Ni_3Si precipitate maintains convex faces.* Moreover, the shape

parameter ρ^* tends toward a constant value in time, as seen in Figure 8(d). This suggests that the growth becomes self-similar at large times for this value of the flux J . Such self-similar growth under constant-flux conditions has been observed in the absence of elasticity by Cristini and Lowengrub.^[10,11] Indeed, recall that in the absence of elasticity, the value of the flux $J = 81$ corresponds to the self-similar flux for a spherical shape perturbed by a four-fold spherical harmonic.^[10]

VI. DISCUSSION AND CONCLUSIONS

We have presented a numerical sharp-interface method, to track the diffusional evolution of a precipitate in three dimensions. While such methods have been developed in two dimensions, they have, to date, proven too costly for three-dimensional simulations.

Most of the difficulty in simulating microstructural evolution using sharp-interface models in three dimensions involves discretizing the moving interface and solving the boundary integral equations for elasticity. Some features of the boundary integral collocation method used in the present work are that (1) the approximation of the surface

*We note that because the adaptive-mesh algorithm adds or subtracts elements only when the curvature changes, the number of elements needed to resolve the Ni_3Al particle increases in time, while the number of elements for the Ni_3Si particle remains constant after a brief initial transient.

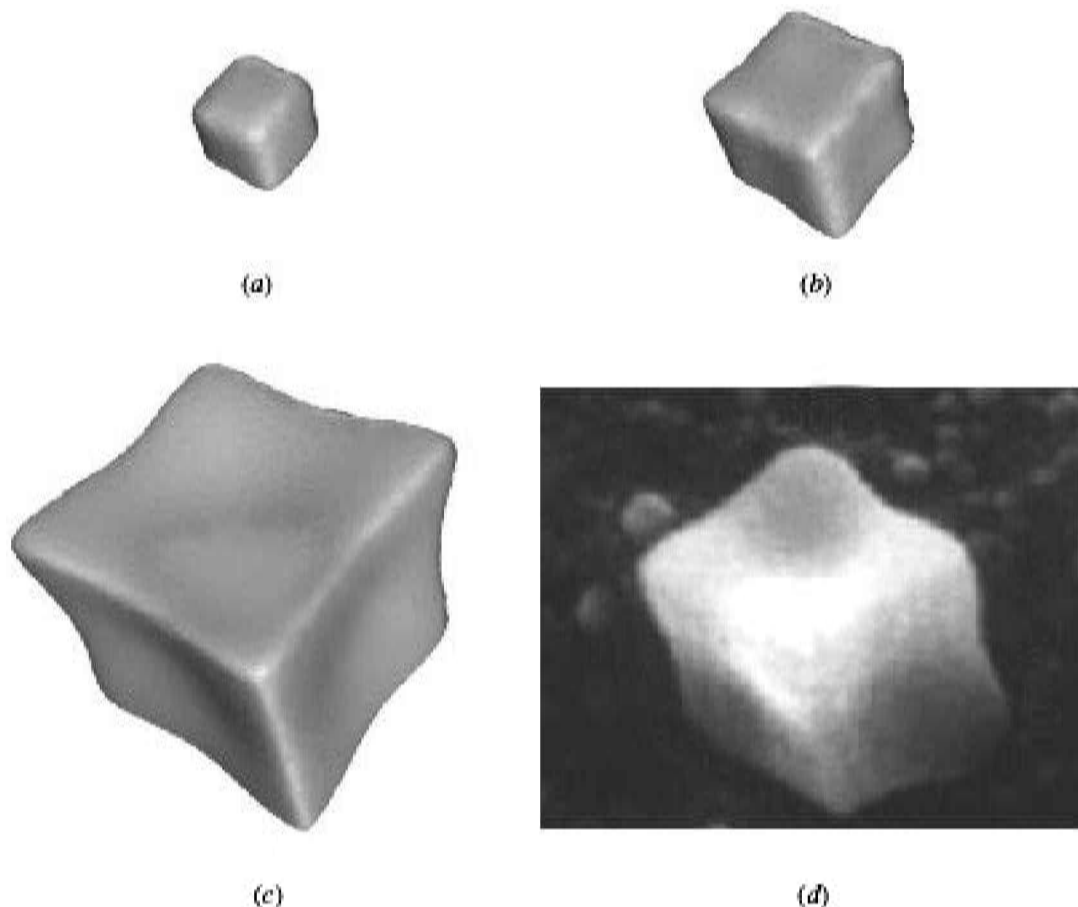


Fig. 7—(a) through (c) A time sequence of the growth of Ni_3Al precipitates in a nickel matrix for the flux $J = 81$, $Z = 4$, and the misfit $\epsilon^T = \text{diag}(1, 1, 1)$. The initial shape is a unit sphere. The cubic axes are normal to the sides of the growing cuboids so that the corners are in the cube diagonal directions. (d) An image taken from an experiment^[32] showing Ni-based precipitates with concave faces similar to those observed in our simulation.

and surface quantities are conducted *via* second-order Lagrangian interpolation; (2) accurate integration quadratures are used for singular, nearly singular, and regular integrals, respectively; (3) an adaptive surface mesh, which optimizes the local-mesh density according to the surface curvature, is used; and (4) efficient parallelization is implemented.

The code is validated for isotropic elasticity by comparing simulation results for long-term coarsened shapes with the equilibrium-shape analysis of Johnson and Cahn. We also compute growing shapes for isotropic elasticity under both constant far-field flux and far-field composition conditions. The shapes rapidly become nonlinear, and the constant-composition morphology is more complex than the constant-flux morphology. This is consistent with the theory developed in Reference 10.

In elastically anisotropic systems, we confirm that our simulation results for long-term coarsened shapes are consistent with the equilibrium-shape calculations of Mueller and Gross.^[7,8] We also consider a coarsened precipitate, where the cubic axes of the precipitate are different from those of the matrix. Our results suggest that there may be more than one minima in the energy, and, so, the observed shape will depend on the growth path. Finally, we simulate growth of precipitates under constant-flux conditions. In the

case of a soft Ni_3Al precipitate in a nickel matrix, we find nonconvex precipitate shapes consistent with experimental observations. In the case of a hard Ni_3Si precipitate grown under the same conditions, we find self-similar growth of a convex shape.

We believe that the three-dimensional boundary integral method with interface tracking presented here is the state of the art. Sharp-interface simulations allow for a very accurate description of interface geometry, as well as precise control over the equations governing particle growth and elasticity. The extension of this method to systems containing multiple precipitates is straightforward but costly. The efficiency of the method can be improved by using the fast multipole method^[33] and by approximating the long-range diffusion and elastic interactions (*e.g.*, Reference 34 in two dimensions). This is currently under study.

ACKNOWLEDGMENTS

The first author (XL) gratefully acknowledges the support of a National Science Foundation SCREMS grant. The second (JL) and fourth (VC) authors acknowledge the support of the National Science Foundation. VC also

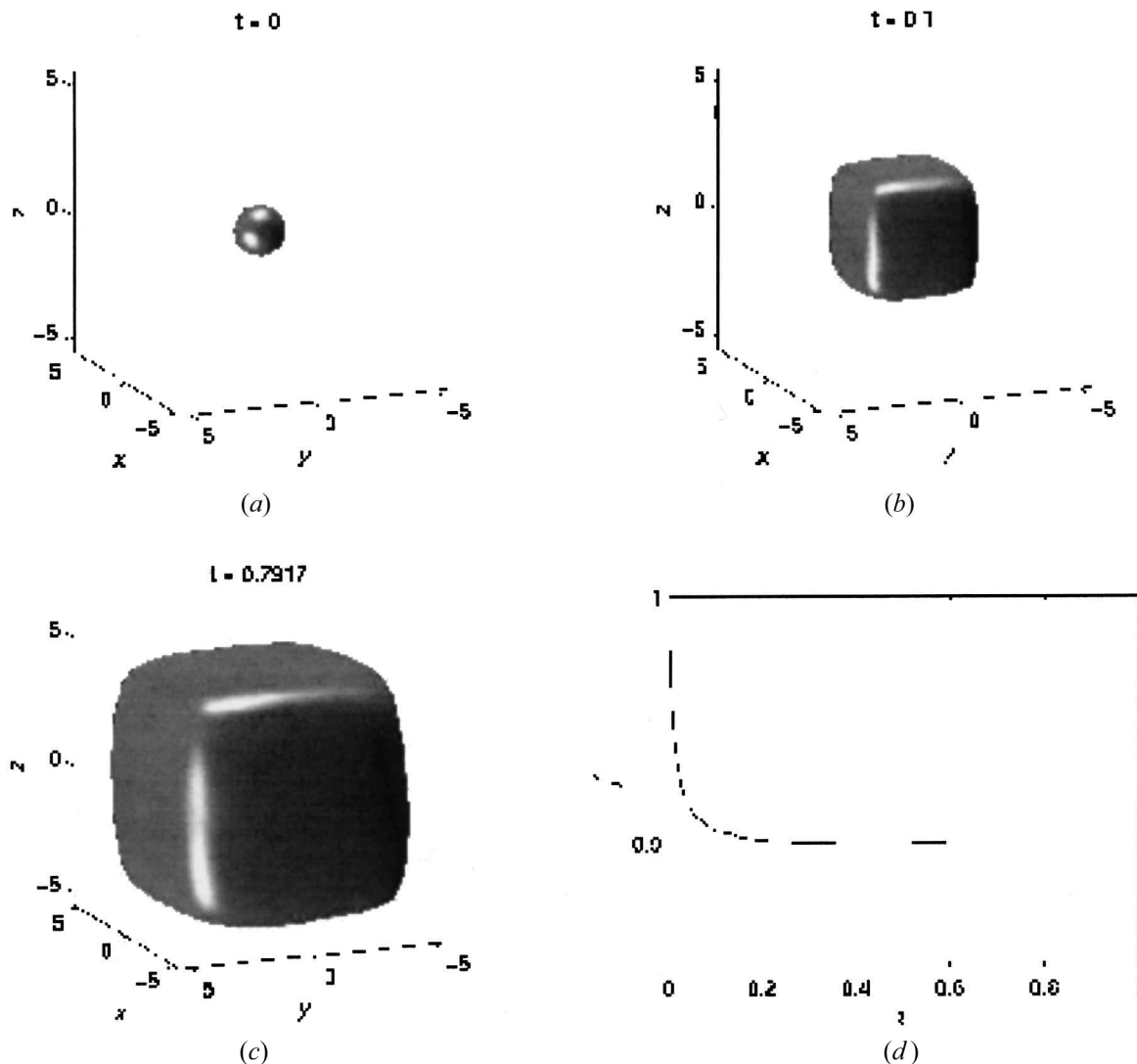


Fig. 8—(a) through (c) A time sequence of the growth of a Ni_3Si precipitate in a nickel matrix for the flux $J = 81$, $Z = 4$, and the misfit $\epsilon^T = \text{diag}(1, 1, 1)$. The initial shape is a unit sphere. (d) The corresponding evolution of the shape parameter ρ^* .

acknowledges the support of the Minnesota Supercomputer Institute Fellowship. The third author (QN) acknowledges the support of the National Science Foundation through both an individual grant and a SCREMS grant. The fifth author (PHL) acknowledges the support of the Division of Materials Science at the Department of Energy through Grant No. DE-FG02-99ER45770. All the authors gratefully acknowledge the support of the Institute of Math and Applications and the Minnesota Supercomputer Institute.

REFERENCES

1. Y. Wang and A. Khachaturyan: *Acta Mater.*, 1997, vol. 45, p. 759.
2. D. Orlikowski, C. Sagui, A. Somoza, and C. Roland: *Phys. Rev. B*, 1999, vol. 8646.
3. L.-Q. Chen: *Ann. Rev. Mater. Res.*, 2002, vol. 32, p. 113.
4. Jong K. Lee: *Mater. Sci. Eng. A*, 1997, vol. A238, p. 1.
5. Jong K. Lee: *Mater. Trans. JIM*, 1998, vol. 39, p. 114.
6. M. Thompson and P. Voorhees: *Acta Mater.*, 1999, vol. 47, p. 983.
7. R. Mueller and D. Gross: *Comput. Mater. Sci.*, 1998, vol. 11, p. 35.
8. R. Mueller and D. Gross: *Comput. Mater. Sci.*, 1999, vol. 16, p. 53.
9. H.-J. Jou, P. Leo, and J. Lowengrub: *J. Comput. Phys.*, 1999, vol. 131, p. 109.
10. V. Cristini and J. Lowengrub: *J. Cryst. Growth*, 2002, vol. 240, p. 267.
11. V. Cristini and J. Lowengrub: unpublished research, University of Minnesota, 2003.
12. J.D. Eshelby: in *Progress in Solid Mechanics 2*, I.N. Sneddon and R. Hill, eds., North-Holland, Amsterdam, 1961, p. 89.
13. P. Leo, J. Lowengrub, and Q. Nie: *J. Comp. Phys.*, 2000, vol. 157, p. 44.
14. J. Zhu, X. Chen, and T.Y. Hou: *J. Comp. Phys.*, 1996, vol. 127, p. 246.
15. A. Greenbaum, L. Greengard, and A. Mayo: *Physica D*, 1992, vol. 60, p. 216.
16. F.J. Rizzo and D.J. Shippy: *J. Comp. Mater.*, 1970, vol. 4, p. 36.
17. A.E.H. Love: *A Treatise on the Mathematical Theory of Elasticity*, Dover, New York, NY, 1944.
18. T. Mura: *Micromechanics of Defects in Solids*, Martinus Nijhoff Publishers, The Hague, 1982.
19. D. Barnett: *Phys. Status Solidi*, 1972, vol. 40, p. 741.
20. D. Barnett, D. Bacon, and R. Scattergood: *Progr. Mater. Sci.*, 1979, vol. 23, p. 51.
21. Xiaofan Li, R. Charles, and C. Pozrikidis: *J. Fluid Mech.*, 1996, vol. 320, p. 395.

22. V. Cristini, J. Blawdziewicz, and M. Loewenberg: *Phys. Fluids*, 1998, vol. 10, 1781.
23. V. Cristini, J. Blawdziewicz, and M. Loewenberg: *J. Comp. Phys.*, 2001, vol. 168, p. 445.
24. Y. Saad and M.R. Schultz: *SIAM J. Sci. Stat. Comput.*, 1986, vol. 7, p. 856.
25. K.E. Atkinson: *The Numerical Solution of Integral Equations of the Second Kind*, Cambridge University Press, United Kingdom, 1997.
26. A.Z. Zinchenko, M.A. Rother, and R.H. Davis: *Phys. Fluids*, 1997, vol. 9, p. 1493.
27. A. Stroud: *Approximate Calculation of Multiple Integrals*, Prentice-Hall, Englewood Cliffs, NJ, 1971.
28. D.M. Barnett, J.K. Lee, H.I. Aaronson, and K.C. Russell: *Scripta Metall.*, 1974, vol. 8, p. 1447.
29. W.C. Johnson and J.W. Cahn: *Acta Mater.*, 1984, vol. 32, p. 1925.
30. P. Leo and H.-J. Jou: *Acta Metall.*, 1993, vol. 41, p. 2271.
31. S.V. Prikhodko, J.D. Carnes, D.G. Isaak, and A.J. Ardell: *Scripta Mater.*, 1997, vol. 38, p. 67.
32. Y.S. Yoo, D.Y. Yoon, and M.F. Henry: *Met. Mater.*, 1995, vol. 1, p. 47.
33. H. Cheng, L. Greengard, and V. Rokhlin: *J. Comp. Phys.*, 1999, vol. 155, p. 468.
34. N. Akaiwa, K. Thornton, and P. Voorhees: *J. Comp. Phys.*, 2001, vol. 173, p. 61.